Spectroscopic and quantum chemical study of an alkaloid aristolochic acid I

ARTICLE *in* SPECTROCHIMICA ACTA PART A MOLECULAR AND BIOMOLECULAR SPECTROSCOPY · JULY 2013

Impact Factor: 2.35 · DOI: 10.1016/j.saa.2013.07.036 · Source: PubMed

5 AUTHORS, INCLUDING:

Bhawani Datt Joshi
Tribhuvan University
16 PUBLICATIONS **36** CITATIONS
SEE PROFILE

Dr. Anubha Srivastava
University of Lucknow
22 PUBLICATIONS **111** CITATIONS
SEE PROFILE

Poonam Tandon
University of Lucknow
206 PUBLICATIONS **973** CITATIONS
SEE PROFILE

Sudha Jain
University of Lucknow
41 PUBLICATIONS **226** CITATIONS
SEE PROFILE

Spectrochimica Acta Part A: Molecular and Biomolecular Spectroscopy 116 (2013) 258–269

Contents lists available at ScienceDirect

Spectrochimica Acta Part A: Molecular and Biomolecular Spectroscopy

journal homepage: www.elsevier.com/locate/saa

Spectroscopic and quantum chemical study of an alkaloid aristolochic acid I

Bhawani Datt Joshi [a,b], Anubha Srivastava [a], Vineet Gupta [a], Poonam Tandon [a,*], Sudha Jain [c]

[a] Department of Physics, University of Lucknow, Lucknow 226007, India
[b] Department of Physics, Siddhanath Sc. Campus, Tribhuvan University, Nepal
[c] Department of Chemistry, University of Lucknow, Lucknow 226007, India

HIGHLIGHTS

- FT-IR and Raman data were recorded and computed with the theoretical results.
- Computations were performed for monomer and the dimer of AA I.
- NBO analysis was performed to elucidate the charge delocalization properties.
- The TD-DFT/6-31G method (IEF-PCM) was employed for assignment of electronic excitations.
- Variation of thermodynamic properties with temperature and DSC analysis has been given.

GRAPHICAL ABSTRACT

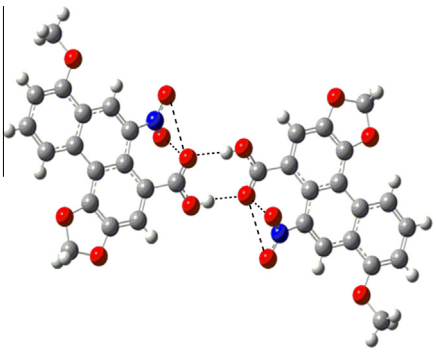

ARTICLE INFO

Article history:
Received 4 March 2013
Received in revised form 10 July 2013
Accepted 21 July 2013
Available online 27 July 2013

Keywords:
AA I
IR
Raman
UV–vis spectroscopy
NBO
Ab initio and DFT

ABSTRACT

Aristolochic acids (AAs) (Aristolochiaceae) are used in the traditional Chinese herb medicine. We have presented the geometry optimization, electrostatic potential surface, frontier orbital energy gap and vibrational wavenumbers of aristolochic acid I (AA I) using *ab initio* Hartree–Fock (HF) and density functional theory (DFT/B3LYP) method employing 6-311G(d,p) basis set. A complete vibrational assignment has been done on the basis of calculations on monomer and dimer of AA I. The UV–vis absorption spectrum has been recorded in ethanol solvent and compared with the calculated one in the gas phase as well as in solvent environment (integral-equation formalism polarizable continuum model; IEF-PCM) using TD-DFT/6-31G basis set. A short outline of the NBO analysis segment with their structural meaning has been presented. The variation of thermodynamic properties with temperature was calculated theoretically and the thermal response of the compound has been recorded with the help of differential scanning calorimetry (DSC) in N_2 environment.

Introduction

Medicinal plants have always had an important place in the therapeutic armoury of mankind. Plant alkaloids one of the most interesting naturally occurring substance, offer many important problems to the chemists for new discoveries. *Aristolochia* species has been used extensively in the traditional discipline. Therefore, this study concentrates on aristolochic acids (3-hydroxy-4-methoxy-10-nitrophenanthrene-1-carboxylic acid methyl ester). Aristolochic acids (AAs), commonly used in Chinese herb medicine, are mainly found in the *Aristolochiaceae* family of plants, including *Aristolochia* and *Asarum*, and have been used extensively in the traditional discipline [1]. Traditional Chinese medicines have been used for clinical treatment even two thousand years back. AAs, mainly include aristolochic acid I (AA I; the most abundant) and aristolochic acid II (AA II), are normally found in almost all

* Corresponding author. Tel.: +91 522 2782653; fax: +91 522 2740840.
E-mail addresses: poonam_tandon@yahoo.co.uk, poonam_tandon@hotmail.com (P. Tandon).

1386-1425/$ - see front matter © 2013 Elsevier B.V. All rights reserved.
http://dx.doi.org/10.1016/j.saa.2013.07.036

Aristolochia species. Their roots have biological functions including treatment of stomach-ache, hypertension relief, leukocyte enhancement, rheumatism relief, edema therapy, toothache, eczema, poisonous snake bites as well as analgesic and diuretic effects [2–5]. However, they have some toxic properties; such as mutagenicity, carcinogenicity and nephrotoxicity in human and may cause the renal failure [6,7]. In oriental medicine the fruit of *Aristolochia* is given for cough and dyspnea. It is believed that the binding of AAs to the exocyclic amino group of purine nucleotides in DNA can cause disease like: mutagenicity and carcinogenicity [8,9]. The early reports of *Aristolochia* medicine confirm its use for the purposes weight control, pain relief and hepatitis induced renal failure [10,11]. The "nitro" group (NO_2) in the ring R3 position and the "methoxyl" (OCH_3) group in the ring R4 position (Fig. 1), are critical in determining maximum toxicity. Any modification of the AA I structure drastically reduces its cytotoxic effect. Reports support that the process of nitro-reduction losses the cytotoxic affect of AA I [12].

Although, X-ray diffraction method is one of the most frequently applied technique but the use of vibrational spectroscopy is also gaining increasing attention in molecular characterization. The X-ray diffraction techniques are sensible to the long-range order while vibrational spectroscopy [13] is applicable to the short-range structure of molecular solids. Vibrational spectroscopy is highly sensitive to the structural changes and is useful for the study of the pharmacological properties [14,15].

In the recent years there has been increasing interest in the application of *ab initio* and density functional theory (DFT) calculations to pharmaceutical drugs [16–19], which provide important clues and additional interpretation of the vibrational spectroscopic data to understand the structure–activity relationship. Our past experience shows that the DFT can be used satisfactorily for vibrational analysis of large molecules [20–23]. Hence, the Raman and IR spectra of AA I molecule have been recorded and analyzed by comparing them with the calculated ones using *ab initio* Hartree–Fock (HF) and density functional theory (DFT). Moreover, we have interpreted the calculated spectra in terms of the potential energy distribution (PED) and made the assignments of the observed bands using PED analysis results. Information about the geometry and structure of the molecule and its molecular electrostatic potential surfaces (MESP) are useful for understanding the relationship between molecular structure and biological activity.

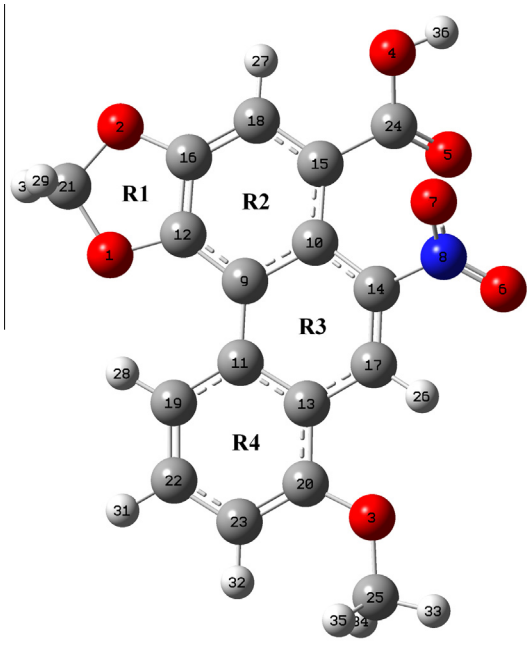

Fig. 1. Optimized ground state structure of AA I.

The interpretation of the UV–vis absorption spectra have been made with highest molecular orbital (HOMO) and lowest unoccupied molecular orbital (LUMO) analysis. The HOMO–LUMO also helps to elucidate charge transfer property within the molecule. The electronic absorption has been recorded in ethanol solvent and compared with the theoretical results in gas phase as well as in the solvent environment. The change in electron density (ED), charge delocalization between the bonding and antibonding orbitals together with the stabilization energies $E^{(2)}$ have been calculated by natural bond orbital (NBO) analysis using the DFT method. Differential scanning calorimetry (DSC) has been performed to achieve the thermal response. The variation of different thermodynamic properties with the temperature has also been reported.

Experimental details

Infrared spectra were recorded on a Bruker TENSOR 27 FT-IR spectrometer with a spectral resolution of 4 cm^{-1} in the region 400–4000 cm^{-1}. KBr pellets of solid samples were prepared from mixtures of KBr and the sample in 200:1 ratio using a hydraulic press. Multi-tasking OPUS software was used for base line corrections.

The FT-Raman spectra were recorded on a Perkin–Elmer 2000R spectrometer as powder sealed in a capillary tube in the region 100–3500 cm^{-1}. The 1064 nm line of an Elforlight Model L04-2000S Nd:YAG laser was used as the exciting source with an output power of about 100 mW at the sample position. All spectra were accumulated for 100 scans with a resolution of 4 cm^{-1}.

The ultraviolet absorption spectra of AA I were examined in the range 200–800 nm using a Varian – Cary 50, UV–visible spectrophotometer equipped with a 10 mm quartz cell. The UV pattern was taken from a 10^{-5} M solution of AA I, dissolved in ethanol at 20 °C.

DSC (Mettler Toledo, Switzerland) operating with version 5.1 of Star^e software was used for melting. The sample (4.23 mg) was encapsulated in aluminum pan having pierced lids to allow escape of volatiles. The heating rates of 10 °C min^{-1} and nitrogen purge at 30 ml min^{-1} were employed. The temperature axis and the cell constant were calibrated using indium.

Computational details

Geometry optimization, an important issue in molecular mechanics, was performed as the first task of the computational work for the AA I molecule taking the parameters from the X-ray diffraction data [24]. It requires in particular the sensitivity of the interaction energy with respect to the change of the molecule's shape which is in general induced by the movement of the nuclei positions. The optimized ground state molecular structure is shown in Fig. 1. The molecular structure, vibrational frequencies and energies of the optimized geometries of AA I were computed by DFT [25] and HF methods using Gaussian 09 [26] program package employing 6-311G(d,p) basis set (both for the monomer and the dimer) based on Becke's three parameters (local, non-local, Hartree–Fock) hybrid exchange functional with Lee–Yang–Parr correlation functional (B3LYP) [27–29]. The basis set 6-311G(d,p) augmented by 'd' polarization functions on heavy atoms and 'p' polarization functions on hydrogen atoms as well as diffuse functions for both hydrogen and heavy atoms were used [30,31]. The absolute Raman intensities and IR absorption intensities were calculated in the harmonic approximation at the same level of theory

as used for the optimized geometries associated with each normal mode, respectively. The normal mode analysis was performed and the PED was calculated along the internal coordinates using localized symmetry. For this purpose, a complete set of 102 internal coordinates were defined using Pulay's recommendations [32,33]. The vibrational assignments of the normal modes were made on the basis of the PED calculated by using the program GAR2PED [34]. Raman and infrared spectra were simulated using a pure Lorentzian band profile (FWHM = 8 cm^{-1}) using indigenously developed software. Visualization and confirmation of calculated data were done by using the CHEMCRAFT Program [35]. The thermodynamic properties at different temperatures have been calculated at the same level of theory.

Results and discussions

Geometry optimization

Initial geometry taken from X-ray diffraction data [24] of AA I, was minimized without any constraint to the potential energy surface and the optimized structural parameters were used in the vibrational frequency calculation to characterize all stationary points as minima. The molecular conformation from the crystalline structure, as well as yielded by geometry optimization, exhibits no special symmetries. The molecule aristolochic acid belongs to the C_1 point group. It has no symmetry elements apart from *I*, and has lattice parameters, a = 19.695 Å, b = 9.050 Å, c = 18.986 Å and z = 8 [24]. The phenanthrene ring system and the five membered rings are almost coplanar. Both the carboxyl and nitro groups lying above and below the plane owe steric effects. Although there is some difference between the theoretical and experimental values, the optimized structure parameters produced an experimental molecular structure. Both the optimized and experimental structures of the title molecule were compared by superimposing them using a least-squares algorithm that minimizes the distances between the corresponding non-hydrogen atoms as shown in Fig. S1 (Supplementary material). The hydroxyl group form strong intermolecular hydrogen bonds O—H···O=C with the oxygen atom of carbonyl group (comparison between experimental and calculated hydrogen bond lengths is given in Table S1 (Supplementary material). Also, the oxygen atom of the carbonyl group form intra-molecular bonds C=O···O=N with both the oxygen atoms of the nitro group (O5···O7 = 2.85 Å and O5···O6 = 3.13 Å) and intermolecular hydrogen bonds as shown in Fig. S2 (Supplementary material).

Comparisons of the optimized and experimental structural parameters (bond lengths, bond angles, dihedral angles) of AA I (in monomer basis) have been listed in Table S2 (Supplementary material) in accordance with the atom numbering scheme as given in Fig. 1. The difference between experimental and calculated values of bond lengths is not more than 0.008 Å except the bond lengths O2—C16, O2—C21, O4—C24, O5—C24 and C22—C23 differ by 0.009/0.026, 0.011/0.014, 0.046/0.016,0.023/0.047 and 0.016/0.013 (in Å) in DFT/HF, respectively. The difference between bond angles is not more than 1.0° except the angles O1—C21—O2, C20—C23—C32, O4—C24—C15 and O5—C24—C15 differ by 1.2/1.7°, 2.2/2.5°, 1.6/1.9° and 2.4/1.5° in DFT/HF, respectively. Similarly, the dihedral angles differ not more than 8.0° except the angles C21—O1—C12—C9, C21—O1—C12—C16, C21—O2—C16—C12, C16—O2—C21—O1, C25—O3—C20—C13 and C25—O3—C20—C23 differ by 8.1/9.8°, 11.1/11.9°, 14.6/16.0°, 12.1/13.2°, 13.8/15.4°, 12.2/12.8° and 12.1/11.6° in DFT/HF, respectively.

In case of the dimer, the geometric parameters corresponding to the intermolecular hydrogen bonding/intra-molecular short bonding moieties have been changed by small values in comparison to that of monomer (listed in Table S3). For example, the O—H bond length increases by 0.034186 Å and the angle C24—O—H increases by 5°.

Molecular electrostatic potential surface

In this study, the electrostatic potential (ESP), electron density (ED) and molecular electrostatic potential (MESP) maps for AA I are as shown in Fig. S3a–d (Supplementary material). In ESP, the negative potential is localized near the oxygen atoms and reflects by the yellowish blobs, while the positive potential is localized on the rest surface. However, the ED plot of the title molecule shows uniform distribution. The molecular electrostatic potential (MESP) is a widely used entity in the chemical literature, generally employed as a tool for probing electron rich regions [36–40]. The MESP at a point r in molecular framework with nuclear charges Z_A located at R_A and electron density $\rho(r)$ is given by a relation:

$$V(r) = \sum_A \frac{Z_A}{|\vec{R}_A - \vec{r}|} - \int \frac{\rho(\vec{r}')d\vec{r}'}{|\vec{r}' - \vec{r}|} \quad (1)$$

where N is the total number of nuclei in the molecule. The first term on the right hand side of the above equation represent the contribution due to nucleus and second due to electrons, respectively. When the latter contribution overrides the former one, the net MESP attains a negative value, providing information about electron-rich sites.

There is a strong correlation of dipole moment, electronegativity and partial charges with the MESP. By utilizing quantum mechanical calculations, values could be generated for partial charges for the atoms in a molecule. The greater is the difference in partial charges, the more polar is the molecule. The projections of molecular MESP of AA I along the molecular plane and a perpendicular to the plane are given in Fig. S3c and d (Supplementary material). It provides a visual method to understand the relative polarity of a molecule and serves as a useful quantity to explain hydrogen bonding, reactivity and structure–activity relationship of molecules including biomolecules and drugs [41,42]. It is the potential energy of a proton at a particular location near a molecule. Despite the fact that the molecular charge distribution remains unperturbed through the external test charge (no polarization occurs) the electrostatic potential of a molecule is still a good guide in assessing the molecules reactivity towards positively or negatively charged reactants. The spatial distribution and the values of the electrostatic potential are in fact largely responsible for the binding of a substrate to its receptor binding site. Different values of the electrostatic potential at the surface of a molecule appear with the different colours. In general the attractive potential appears in red colored regions and those of repulsive potential appear in blue. Negative electrostatic potential corresponds to an attraction of the proton by the concentrated electron density in the molecules (from lone pairs, pi-bonds, etc.). Positive electrostatic potential corresponds to repulsion of the proton by the atomic nuclei in regions where low electron density exists and the nuclear charge is incompletely shielded. In the title molecule the space near the oxygen atoms of nitro group and carbonyl group show most negative potential region and the region near hydrogen of hydroxyl group the most positive one. The electron density isosurface is a surface on which the molecule's electron density has a particular value and that encloses a specified fraction of the molecule's electron probability density.

Electronic and UV spectra

The UV–vis absorption spectrum of AA I was measured in ethanol solution and given in Fig. 2. It is observed that the absorption

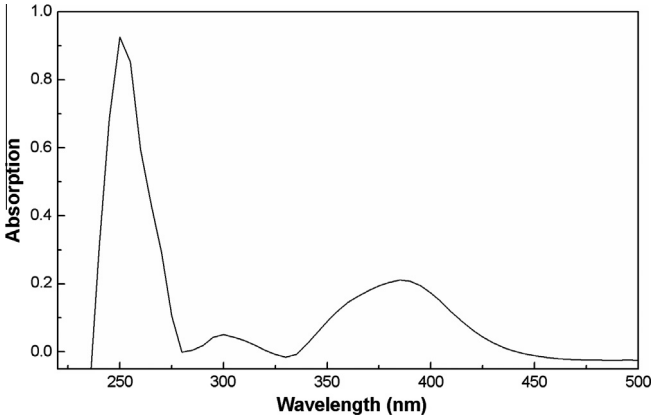

Fig. 2. The electronic absorption UV–vis spectra in the range 200–800 nm of AA I.

bands centered at 385, 300 and 250 nm for ethanol solution. The observed electronic transitions of AA I were computed with the calculated in the gas phase and in the ethanol solution (IEF-PCM model) using the TD-DFT/6-31G method. The HOMO is the outermost (highest energy) orbital containing electrons that could act as an electron donor. The LUMO is the innermost (lowest energy) orbital that has room to accept electrons and can act as the electron acceptor. According to the frontier molecular orbital theory, the formation of a transition state is due to an interaction between the frontier orbitals (HOMO and LUMO) of reactants [43]. The energy of the HOMO is directly related to the ionization potential and the energy of the LUMO is directly related to the electron affinity. High value of HOMO energy is likely to indicate a tendency of the molecule to donate electrons to appropriate acceptor molecule of low empty molecular orbital energy. The lower values of LUMO energy show more probability to accept electrons. So, the gap energy, i.e. the difference in energy between the HOMO and LUMO, is an important stability index. It is a critical parameter in determining molecular electrical transport properties because it is a measure of electron conductivity. Low gap value refers to the higher electronic transition and vice versa. The HOMO–LUMO plot with the frontier orbital energy gap for the title molecule is shown in Fig. S4 (Supplementary material). In HOMO the main electronic transition is occurred at C=C bonds of rings R2, R3 and R4 and carbonyl group (in small amounts), while in LUMO the charge density is mainly accumulated at N—C bond in ring R3 and nitro group.

The calculated frontier orbital energies, absorption wavelengths (λ_{max}), oscillator strengths (f) and excitation energies (E) and dipole moments (μ) for vacuum and ethanol solution are illustrated in Table 1. This electronic absorption corresponds to the transition from the ground to the first excited state and is mainly described by one electron excitation from the HOMO to the LUMO. The first allowed-dipole transition in the gas phase is calculated about 393 nm with oscillator strength 0.0975. The next transitions are calculated about 279, 259, 238 and 224 nm with oscillator strengths 0.1213, 0.1106, 0.1178 and 0.3832, respectively. In the experimental UV spectrum $\pi \rightarrow \pi^*$ and $n \rightarrow \pi^*$ are the main observed transitions. The $n \rightarrow \pi^*$ transition arises due to carbonyl group and observed at about 250 nm. A single band of low intensity in the region 280–330 nm, with no major absorption at shorter wavelengths, usually also indicates an $n \rightarrow \pi^*$ transition.

Natural bond orbital (NBO) analysis

The NBO analysis was performed with the NBO 3.1 program [44]. NBO analysis reveals the electron delocalization and conjugation with the estimation of bond stabilization energy, $E^{(2)}$. The hybridization of atomic lone pairs and of the atoms involved in bond orbitals assigned by the second order micro-perturbation theory, are important data in spectral interpretation since the frequency ordering is related to the bond hybrid composition. The most important interactions between 'filled' (donor) Lewis-type NBOs and 'empty' (acceptor) non-Lewis NBOs are reported and listed in Table 2a. The stabilization energy $E^{(2)}$ resulting on transfer of electrons from the Lewis-type NBOs to non-Lewis-type NBOs is estimated as [45–47]:

$$E(2) = \Delta E_{ij} = q_i[F_{ij}^2/(\varepsilon_j - \varepsilon_i)] \quad (2)$$

where q_i is the donor orbital occupancy, ε_i and ε_j are diagonal elements (orbital energies) and $F(i,j)$ is the off-diagonal NBO Fock or Kohn–Sham matrix element [47].

The hyperconjugative interactions; n(O7) → π*O6—N8, n(O4) → π*O5—C24 and n(O5) → σ*O4—C24 lead to the stabilization energies of 694.80, 170.63, 135.60 kJ/mol, respectively. Another hyperconjugative interactions are formed by overlapping between the bonding σ and antibonding σ* as well as bonding π and antibonding π* orbitals of the fused rings, resulting itra-molecular charge transfer (ICT) that stabilizes the molecular system. The occupancy of σ bonds (1.95512–1.98791) and σ* bonds (0.01954–0.03809) indicates weak charge delocalization leading to the maximum delocalization energy ~26.42 kJ/mol, while the occupancy of π bonds (1.58161–1.98626) and π* bonds (0.23073–0.60410) indicate strong charge delocalization leading to the maximum stabilization energy ~98.48 kJ/mol. Hence, π NBOs have lower occupancies and hence posses more electro donor-ability in comparison to the σ NBOs. Further, the occupancy of natural bonds and lone pairs, and the percentage of p-character calculated by NBO analysis method are given in the Table 2b. In this Table, the

Table 1
Electronic transitions, absorption wavelength λ_{max} (nm), excitation energy (eV), oscillator strengths (f), frontier orbital energies (eV) and dipole moment (Debye) of AA I.

Excited state	Experimental	Calculated								Transition type/assignments
	AA	Gas phase				Ethanol				
	λ_{max} (nm)	Transitions	E (eV)	f	λ_{max} (nm)	Transitions	E (eV)	f	λ_{max} (nm)	
1	385	H → L	3.1563	0.0975	393	H → L	2.8607	0.0959	433	π → π*
2		H → L+1	3.6532	0.0617	339	H → L+1	3.2223	0.1250	385	
3		H → L+2	3.9789	0.0889	312	H → L+2	3.7896	0.0644	327	
4	300	H−2 → L	4.4401	0.1213	279	H−1 → L+1	4.0433	0.0815	307	π → π*
5		H−1 → L+2	4.5934	0.0735	270	H−2 → L	4.2606	0.0992	291	
6	250	H−2 → L+1	4.7840	0.1106	259	H−1 → L+2	4.4390	0.0700	279	π → π*
7		H−3 → L+1	5.2125	0.1178	238	H−2 → L+1	4.7180	0.1582	263	
8		H−1 → L+3	5.3171	0.0671	233	H−3 → L+1	5.3271	0.1090	233	
9		H−2 → L+2	5.5474	0.3832	224	H−2 → L+2	5.4089	0.5166	229	

	E_{HOMO} (eV)	E_{LUMO} (eV)	ΔE (eV)	μ (D)
Gas	−5.88601278	−2.23704294	3.64896984	7.2550
Ethanol	−5.78552625	−2.38928289	3.39624336	9.1082

Table 2a
Second order perturbation theory analysis of Fock matrix in NBO basis.

Donor NBO (*i*)	ED (e)	Acceptor NBO (*j*)	ED (e)	$E^{(2)}$.[a] (kJ/mol)	$[E(j)-E(i)]$[b] (a.u.)	$F(i,j)$[c] (a.u.)
σO1—C21	1.98791	σ*C9—C12	0.02786	20.86	1.37	0.074
σO1—C21	1.98791	σ*C16—C18	0.02311	20.31	1.40	0.074
σC9—C10	1.95512	σ*O1—C12	0.02838	25.16	0.99	0.069
σC9—C12	1.96682	σ*C12—C16	0.03809	22.40	1.26	0.074
σC10—C14	1.96772	σ*C14—C17	0.01954	22.70	1.30	0.075
σC12—C16	1.97679	σ*C9—C12	0.02786	25.29	1.27	0.078
σC15—C18	1.96382	σ*O2—C16	0.02974	25.16	1.03	0.071
		σ*C10—C15	0.02836	20.27	1.24	0.070
σC14—C17	1.97097	σ*C10—C14	0.03187	23.20	1.24	0.074
σC16—C18	1.97186	σ*C12—C16	0.03809	22.40	1.28	0.074
σC17—H26	1.97205	σ*C10—C14	0.03187	26.42	1.02	0.072
σC18—H27	1.97521	σ*C10—C15	0.02836	21.23	1.07	0.066
σC20—C23	1.97874	σ*C13—C20	0.03205	20.98	1.24	0.071
σC22—H23	1.97418	σ*O3—C20	0.02990	21.23	1.06	0.065
πO6—N8	1.98626	LP(3)O7	1.44314	59.90	0.18	0.084
πC9—C10	1.58161	π*C11—C13	0.44925	71.23	0.28	0.062
		π*C12—C16	0.40107	98.48	0.26	0.071
		π*C14—C17	0.23073	57.18	0.29	0.059
		π*C15—C18	0.36675	75.45	0.28	0.064
πC11—C13	1.59104	π*C9—C10	0.47282	65.46	0.27	0.059
		π*C14—C17	0.23073	75.74	0.29	0.06
		π*C19—C22	0.28832	64.92	0.29	0.061
		π*C20—C 23	0.34485	86.32	0.27	0.068
π*C12—C16	1.64081	σ*C16—C18	0.02311	24.16	1.30	0.078
		π*C9—C10	0.47282	72.65	0.30	0.067
		π*C15—C18	0.36675	84.85	0.31	0.071
πC14—C17	1.76360	π*O 6—N8	0.60410	71.94	0.16	0.053
		π*C9—C10	0.47282	59.36	0.29	0.061
		π*C11—C13	0.44925	53.13	0.31	0.059
πC15—C18	1.68476	π*O5—C24	0.24092	71.69	0.30	0.065
		π*C9—C10	0.47282	77.50	0.28	0.067
		π*C12—C16	0.40107	87.65	0.27	0.069
πC19—C22	1.70518	π*C11—C13	0.44925	83.98	0.28	0.070
		π*C20—C23	0.34485	67.97	0.28	0.061
πC20—C23	1.69325	π*C11—C13	0.03017	62.41	0.30	0.062
		π*C19—C22	0.28832	87.19	0.30	0.072
LP(2)O1	1.85394	π*C12—C16	0.40107	96.85	0.35	0.086
		σ*C21—H29	0.03746	24.20	0.70	0.058
LP(2)O2	1.85768	π*C12—C16	0.40107	97.81	0.35	0.086
		σ*C21—H29	0.03746	26.58	0.69	0.061
LP(2)O3	1.83383	σ*C20—C23	0.02697	29.01	1.12	0.079
		π*C20—C23	0.34485	134.85	0.35	0.099
		σ*C25—H34	0.01811	22.70	0.70	0.057
		σ*C25—H35	0.01817	22.36	0.70	0.057
LP(1)O4	1.97851	σ*O5—C24	0.02614	24.79	1.21	0.076
LP(2)O4	1.82189	π*O5—C24	0.24092	170.63	0.37	0.111
LP(1)O5	1.97633	RY*(1) C24	0.02009	66.38	1.59	0.142
LP(2)O5	1.83903	σ*O4—C24	0.09886	135.60	0.61	0.128
		σ*C15—C24	0.06747	77.12	0.68	0.102
LP(2)O6	1.89453	σ*C7—N8	0.07084	80.30	0.71	0.105
		σ*N8—C14	0.10925	59.36	0.56	0.079
LP(2)O7	1.89455	σ*N8—C14	0.10925	77.66	0.73	0.105
		π*C14—C17	0.23073	53.21	0.56	0.075
LP(3)O7	1.44314	π*O6—N8	0.60410	694.80	0.15	0.143
		σ*O7—N8	0.07084	32.98	0.69	0.076

$E^{(2)}$ > 20 kJ/mol.
[a] $E^{(2)}$ means energy of hyper conjugative interaction (stabilization energy).
[b] Energy difference between donor and acceptor *i* and*j* NBO orbitals.
[c] $F(i,j)$ is the Fock matrix element between *i* and *j* NBO orbitals.

s- and p-characters of selected Lewis orbitals are listed, which are involved in the valence hybrids. For example, the p-character of LP(3)O7 and LP(2)O7 are 99.12% and 99.89%, respectively. Lower occupancy of bonding NBOs means more electrons have been donated to the anti-bonding NBOs [48], thus lower occupancy leads to stronger donor ability.

Thermodynamic properties and thermal analysis

On the basis of vibrational analyses and statistical thermodynamics, the standard thermodynamic functions: heat capacity ($C^{\circ}_{p,m}$), entropy (S°_{m}) and enthalpy (H°_{m}) were obtained and listed in Table 3a. As observed from this Table, the values of heat capacity, entropy and enthalpy all increase with the increase of temperature from 100 K to 600 K which is attributed to the enhancement of molecular vibration while the temperature increases. The correlation between these thermodynamic properties and temperatures are shown in Fig. 3. The correlation equations for AA I are as follows:

$$H^{\circ}_{m} = Y = 664.1776 + 0.14251T + 3.31434x10^{-5}T^{2} \quad (R^{2} = 0.97333)$$
$$S^{\circ}_{m} = Y = 274.2365 + 1.12744T - 1.03268x10^{-4}T^{2} \quad (R^{2} = 0.97986)$$
$$C^{\circ}_{p,m} = Y = 22.39441 + 1.11599T - 3.97347x10^{-4}T^{2} \quad (R^{2} = 0.99680)$$

Table 2b
Selected Lewis orbitals (occupied bond or lone pair) with the valence hybrids corresponding to the various interactions in (3): A – donor, B – acceptor and (ED) – Electron density.

Bond (A—B)	ED_{A-B}	ED_A (%)	ED_B (%)	NBO Hybrid orbitals	s (%)	p (%)
σO1—C12	1.98569	67.44	32.56	$0.8212(sp^{2.15})_O$+	31.72	68.21
				$0.5707(sp^{3.23})_C$	23.61	76.16
σO1—C21	1.98791	68.53	31.47	$0.8278\ (sp^{2.96})_O$+	25.20	74.72
				$0.5610(sp^{3.48})_C$	22.24	77.44
σO2—C16	1.98522	67.13	32.87	$0.8193(sp^{2.19})_O$+	31.33	68.60
				$0.5734(sp^{3.16})_C$	24.00	75.78
σO2—C21	1.98845	67.86	32.14	$0.8238(sp^{2.98})_O$+	25.10	74.81
				$0.5669(sp^{3.38})_C$	22.77	76.91
σO3—C20	1.99031	67.69	32.31	$0.8227(sp^{1.90})_O$+	34.42	65.51
				$0.5685(sp^{3.05})_C$	24.67	75.11
σO3—C25	1.99156	68.56	31.44	$0.8280(sp^{2.55})_O$+	28.16	71.78
				$0.5607(sp^{3.49})_C$	22.22	77.51
σO4—C24	1.99462	68.67	31.33	$0.8287(sp^{1.88})_O$+	34.68	65.24
				$0.5598(sp^{2.70})_C$	26.97	72.80
σO4—H36	1.98636	74.59	25.41	$0.8637(sp^{3.81})_O$+	20.77	79.14
				$0.5040(sp^{0.00})_H$	99.83	0.17
σO5—C24	1.99480	65.64	34.36	$0.8102(sp^{1.46})_O$+	40.58	59.31
				$0.5862(sp^{2.04})_C$	32.81	67.04
πO5—C24	1.98442	69.86	30.14	$0.8358(sp^{71.16})_O$+	1.38	98.50
				$0.5490(sp^{99.99})_C$	0.94	98.56
σO6—N8	1.99476	51.67	48.33	$0.7188\ (sp^{2.81})_O$+	26.20	73.66
				$0.6952(sp^{2.13})_N$	31.89	67.98
πO6—N8	1.98626	59.62	40.38	$0.7721(sp^{99.99})_O$+	0.03	99.82
				$0.6355(sp^{99.99})_N$	0.38	99.35
σO7—N8	1.99214	51.83	48.17	$0.7200(sp^{3.02})_O$+	24.84	75.0
				$0.6940(sp^{2.15})_N$	31.75	68.12
σN8—C14	1.98735	62.55	37.45	$0.7909(sp^{1.80})_N$+	35.68	64.28
				$0.6119(sp^{3.21})_C$	23.71	76.17
LP(1)O1	1.96272	–	–	$sp^{1.33}$	1.96	57.08
LP(2)O1	1.85394	–	–	$sp^{99.99}$	0.17	99.78
LP(1)O2	1.96221	–	–	$sp^{1.30}$	43.45	56.52
LP(2)O2	1.85768	–	–	$sp^{99.99}$	0.09	99.85
LP(1)O3	1.96194	–	–	$sp^{1.67}$	37.40	62.57
LP(2)O3	1.83383	–	–	p	–	99.95
LP(1)O4	1.97851	–	–	$sp^{1.25}$	44.53	55.44
LP(2)O4	1.82189	–	–	p	–	99.94
LP(1)O5	1.97633	–	–	$sp^{0.72}$	58.01	41.97
LP(2)O5	1.83903	–	–	p	–	99.92
LP(1)O6	1.98095	–	–	$sp^{0.35}$	73.86	26.14
LP(2)O6	1.89453	–	–	p	–	99.93
LP(1)O7	1.97888	–	–	$sp^{0.34}$	74.43	25.56
LP(2)O7	1.89455	–	–	p		99.89
LP(3)O7	1.44314	–	–	p		99.12

Table 3a
Theoretically calculated thermodynamic properties at different temperatures using 6-311G(d,p) basis set.

Temperature (K)	Enthalpy (kJ/mol)	Specific heat (J/mol K)	Entropy (J/mol K)
100	686.05504	130.63754	374.7161
150	693.82148	179.49756	440.4006
200	703.99142	227.36692	500.973
250	716.56904	275.65846	558.749
300	731.55016	323.49438	614.7651
350	748.88462	369.49946	669.4019
400	768.4512	412.53674	722.6969
450	825.24904	422.34302	688.4335
500	813.58266	487.50922	824.9439
550	838.76716	519.36918	873.7245
600	865.46064	547.80572	920.8791

These equations can be used for the further studies on the title compound. For instance, when the interaction of title compound with another compound is studied, these thermodynamic properties can be obtained from the above equations and then can be used to calculate the change in Gibbs free energy of the reaction, which will in turn help to judge the spontaneity of the reaction. Scale factors have been recommended [26] for an accurate prediction in determining the zero-point energies, heat capacities, entropies, enthalpies, Gibbs free energies. All these thermodynamic parameters and dipole moment at room temperature (298.15 K) with DFT/HF methods are also presented in Table 3b.

Differential scanning calorimetry (DSC), a widely used experimentally fundamental tool in thermal analysis, is a technique for the study of a variety of phase transformations of the materials [49–51]. The DSC curve of AA I observed on heating is shown in Fig. 4. The sharp melting endothermic peak during heating was occurred at 268.99 °C (onset–peak–endset) with enthalpy of 448.74 J/g. From the curve it is clear that no glass transition has occurred.

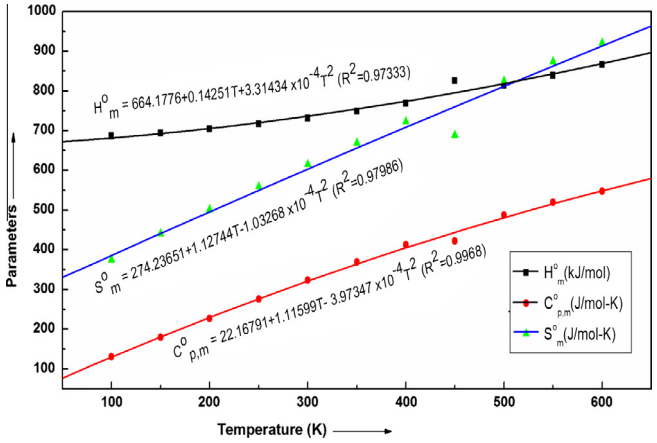

Fig. 3. Correlation graphics of thermodynamic properties and temperature for AA I.

Vibrational assignments

AA I molecule has 36 atoms and hence gives 102 (3N-6) fundamental modes of vibration, while its dimer gives 210 modes. All of them are both the Raman and IR active. Since the vibrational wavenumbers obtained from the DFT calculations are higher than the observed wavenumbers, they were scaled down by the wavenumber linear scaling procedure (WLS) [$\nu_{obs}/\nu_{cal} = (1.0087 - 0.0000163 \times \nu_{cal})\ cm^{-1}$] of Yoshida et al. [52]. However, there are different scaling factors, but the vibrational wavenumbers calculated uniformly scaled with only one scaling factor [53,54] are often in good agreement to the observed ones. All the calculated vibrational wavenumbers reported in this study are the scaled values.

The Raman scattering cross sections, $\partial\sigma_j/\partial\Omega$, which are proportional to the Raman intensities, may be calculated from the Raman scattering amplitude and predicted wavenumbers for each normal modes using the relationship [55,56]

$$\frac{\partial\sigma_j}{\partial\Omega} = \left(\frac{2^4\pi^4}{45}\right)\left(\frac{(\upsilon_0 - \upsilon_j)^4}{1 - \exp\left[\frac{-hc\upsilon_j}{kT}\right]}\right)\left(\frac{h}{8\pi^2 c\upsilon_j}\right)S_j$$

where S_j and υ_j are the calculated scattering activities and the predicted wavenumbers, respectively, of the jth normal mode, υ_0 is the Raman excitation wavenumber and h, c and k are the universal constants.

The calculated Raman and IR intensities were used to convolute each predicted vibrational mode with a Lorentzian line shape with a full width at half maximum (FWHM = 8 cm^{-1}) to produce simulated spectra. Assignments have been made on the basis of relative intensities, energies, line shape and potential energy distribution. All the vibrational bands have been assigned satisfactorily. The assigned wavenumbers of the vibrational modes calculated at the HF and B3LYP level with the basis set 6-311G(d,p) along with their PED are given in Table 4.

Table 3b
Theoretically calculated thermodynamic properties at room temperature using 6-311G(d,p) basis set.

Thermodynamic properties	DFT (B3LYP)	HF
Total energy (eV)	−33630.40853	−33435.57183
Zero-point energy (kJ/mol)	678.6126	726.1323
Rotational constants (GHz)	0.29224	0.29224
	0.20271	0.20271
	0.12406	0.12406
Dipole moment (D)	6.8829	7.7225
Entropy (J/mol K)	612.7169	538.9985
Enthalpy (kJ/mol)	730.9524	770.7042
Specific heat (J/mol K)	321.7471	291.9145

In the AA I molecule, there are four rings with different functional groups as shown in Fig. 1. The vibrational assignments of these rings and some functional groups have been discussed separately on the basis of calculations on monomer and compared with the calculated values for dimer. Out of several internal coordinates that may be present in the PED, we have discussed here only the dominant contributions to the total potential energy of normal modes of vibration. A comparison between observed and calculated (monomer and dimer) IR and Raman spectra is presented in Figs. 5 and 6, respectively.

O—CH_3 vibrations

In a molecule containing a methoxy group, the back donation of electronic charge from lone pair electrons on oxygen atom to the σ^* orbital of C—H bonds weakens the C—H bonds. This is followed by an increase in C—H bond distance and decrease in C—H force constant. This results an enhancement of IR band intensities of C—H stretching modes [57–59]. The CH_3 group has several modes associated with it, such as symmetric and asymmetric stretches, bends, rocks, and torsions. For the CH_3 compounds, the symmetric stretching mode appears in the range 2935–2860 cm^{-1}, where as the asymmetric stretching modes appear in the region 2985–2925 cm^{-1} [60]. In present study, the pure asymmetric stretching modes are calculated at 3009/2945 cm^{-1} in monomer and observed at 3010/2958 cm^{-1} in the IR spectrum and at 2997/2962 cm^{-1} in the Raman spectrum, respectively. In this study, the symmetric stretching mode is calculated at 2888 cm^{-1} which matches well with 2918 cm^{-1} mode in the IR spectrum and at 2891 cm^{-1} in the Raman spectrum. The CH_3 mixed asymmetric deformation is calculated at 1469 cm^{-1} and assigned to the medium intensity band at 1468 cm^{-1} in the IR spectrum and very weak band at 1466 cm^{-1} in the Raman spectrum. The symmetric deforming vibration is calculated at 1477, 1451 and 1447 cm^{-1}, which matches well with medium intensity bands at 1469 and 1450 and very weak band at 1437 cm^{-1} in the IR spectrum as well as at the very weak band at 1468 cm^{-1} and the medium intensity bands 1451 and 1448 cm^{-1} in the Raman spectrum. The rocking modes are calculated at 1192 and 1159 cm^{-1} and have good agreement with the observed spectra. The blue shifting of the methyl stretching wavenumbers are due to the inference of electronic effect resulting from the hyperconjugation and induction of methyl group in-the aromatic ring [61].

The mixed stretching vibrations of C25—O are calculated at 1068/1004 cm^{-1}, and have excellent agreements at 1065/999 and 1067/1001 cm^{-1} with the observed IR Raman spectrum, respectively. Its torsion is calculated at 282 cm^{-1}.

OH vibrations

The O—H stretching vibrations are sensitive to hydrogen bonding. The non-hydrogen bonded (or) free hydroxyl group absorb strongly in 3700–3550 cm^{-1} region, whereas the existence of H-bonding can lower the O—H stretching vibration to the region 3500–3200 cm^{-1} region with increase in IR intensity and breadth [62,63]. In this molecule, there is one OH group connected at the ring R2 through carbonyl. The O—H stretching vibrating is calculated at 3567 cm^{-1} in DFT and observed at very weak intensity band at 3128 cm^{-1} in the IR spectrums, showing a difference of about 439 cm^{-1}. While on moving towards the dimer this mode is calculated at 3047 and 2961 cm^{-1} with very high intensity showing a better agreement with the observed spectra. This large shifting is due to the involvement of this group in the intermolecular

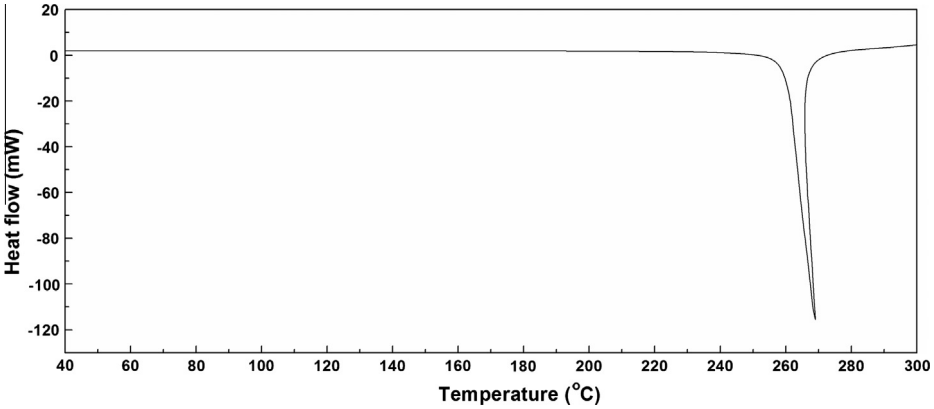

Fig. 4. DSC curve of AAI at heating rate of 10 °C min^{-1} in N_2 atmosphere.

hydrogen bonding interactions. The mixed deformation of this mode is calculated at 1179 cm^{-1} and observed at 1169 cm^{-1} in the IR spectrum and at 1171 cm^{-1} in the Raman spectrum.

C═O vibration

The most of the characteristic features of the carboxylic group are observed usually in 1750–1600 cm^{-1} region [64]. This multiply bonded group (C═O bond by pπ–pπ bonding) is highly polar and therefore gives rise to an intense infrared absorption band. Both the carbon and oxygen atoms have the different electronegativities; as a result the bonding electrons are not equally distributed between the two atoms. In this work, the C═O stretching vibration is calculated at 1764 cm^{-1}, which is assigned with the strong intensity band at 1687 cm^{-1} in the IR and weak intensity band at 1688 cm^{-1} in the Raman spectra, respectively. The difference of ≈77 cm^{-1} in monomer and downshift of 22 cm^{-1} in dimer resulting to a small increase in C═O bond length of 0.01125 Å is reported. The wagging, deformations and rocking of C═O are calculated to be 796, 654 and 423 cm^{-1} showing good agreements with the observed results.

C—NO_2 vibrations

There is one nitro (NO_2) group as a functional group in this molecule. Generally, the asymmetric NO_2 stretching modes are expected in the interval 1600–1500 cm^{-1} and symmetric stretching modes in the interval 1400–1300 cm^{-1} in the IR absorption bands [65]. The asymmetric stretching vibration of N═O is calculated at 1576 cm^{-1}, which matches well with a very weak band at 1541 cm^{-1} in the IR spectrum and the medium intensity band at 1543 cm^{-1} in the Raman spectrum. Symmetric stretching mode, which is mixed with C—C stretching of rings R4 and R3, is calculated at 1361 cm^{-1}, which agrees well with very strong band at 1350 cm^{-1} in both Raman and IR spectra. In general, the strongest band in Raman spectrum is weak in the IR spectrum, but the intramolecular charge transfer through a single-double bond conjugated path can induce large variations of both the molecular dipole moment and the molecular polarizability, that makes both Raman and IR activity strong at the same time [66,67]. The deformation (or scissoring) vibration of NO_2 is calculated at 826 cm^{-1} and observed at the band 830 cm^{-1} in the Raman spectrum and at 813 cm^{-1} in the IR spectrum. The NO_2 wagging mode calculated at 775 cm^{-1} has good agreement with the 777 cm^{-1} band in the IR and 778 cm^{-1} in the Raman spectra, respectively. The NO_2 rocking mode is calculated at 396 cm^{-1}.

Ring R1 vibrations

It is a five membered planer ring having one CH_2 moiety. Basically one can expect six fundamental assignments associated with each CH_2 group vibrations namely, symmetric, asymmetric stretch, deformation and rocking modes which belong to polarized in-plane vibrations. In addition to that, CH_2 wagging and twisting modes would be expected to be depolarized out-of-plane symmetry species. The asymmetric CH_2 stretching vibrations are generally observed in the range of 3000–2900 cm^{-1}, while the symmetric stretch appears in the region 2900–2800 cm^{-1} [68,69]. In this study, the asymmetric stretching vibration is calculated at 2985 cm^{-1} in the scaled DFT and observed at 2993 cm^{-1} in the IR spectrum and 2995 cm^{-1} in the Raman spectrum. Symmetric vibration for this group is calculated at 2886 cm^{-1}, which is observed at the band 2850 cm^{-1} in IR and at 2878 cm^{-1} in the Raman spectra, respectively. The calculated deformation of CH_2 is 1518 cm^{-1}, which has excellent agreements with strong band at 1523 cm^{-1} in the IR spectrum and very weak band at 1507 cm^{-1} in the Raman spectrum. The CH_2 wagging is calculated at 1416 cm^{-1} and observed at 1419 cm^{-1} in the IR spectrum and at 1406 cm^{-1} in the Raman spectrum. The twisting mode is calculated at 1203 cm^{-1}, which matches at 1203 cm^{-1} in the IR spectrum and at 1194 cm^{-1} in the Raman spectrum. The calculated rocking vibrations are 1139/1134 cm^{-1}, which is observed at 1142 cm^{-1} in the Raman spectrum and at 1147/1126 cm^{-1} in the IR spectrum.

Ring R2 vibrations

R2 is an aromatic six membered ring between R1 and R3 having a methine (CH) and a carboxyl (COOH) moiety as functional groups. The characteristic region for the identification of C—H stretching in the heteroaromatic structures is 3100–3000 cm^{-1} [70,71]. In this study, the C—H stretching vibration is calculated at 3086 cm^{-1}. The observed IR/Raman peaks for this mode are at 3080/3082 cm^{-1}. The mixed in-plane deformations are calculated at 1183 cm^{-1} corresponding to the observed very weak bands at 1171 cm^{-1} in the IR spectrum and at 1173 cm^{-1} in the Raman spectrum. The CH out-of-plane deformation is observed at 901 cm^{-1} in the IR and 897 cm^{-1} in the Raman spectrum, respectively. The calculated frequency of this mode is at 896 cm^{-1}.

The C—C stretching vibrations, being mixed with the other rings, are calculated at 1606, 1596, 1383 and 1333 cm^{-1}, which agrees well to the strong bands at 1593 and 1591 cm^{-1} and weak bands at 1372 and 1331 cm^{-1} in the IR spectrum the medium intensity bands at 1593, 1591 and 1372 cm^{-1} and very intense band at 1331 cm^{-1} in the Raman spectrum [67]. The mixed

Table 4
Observed and calculated wavenumbers (in cm^{-1}) AA I monomer and dimer.

Unscaled DFT	Scaled		Experimental		Dimer	PED[a] (%)
	HF	DFT	IR	Raman	Scaled DFT	
3765	3878	3567	3128_{vw}	–	3047, 2961	ν(OH)(100)
3261	3280	3116	3097_{vw}	3132_{vw}	3116, 3116	R4[ν(CH)](98)
3240	3261	3097	3095_{vw}	3098_{vw}	3096, 3096	R3[ν(CH)](98)
3231	3236	3089	3080_{vw}	3082_{vw}	3089, 3089	R2[ν(CH)](99)
3212	3221	3072	3074_{vw}	3074_{vw}	3070, 3070	R4[ν(CH)](99)
3175	3182	3038	–	3030_{vw}	3038, 3038	R4[ν(CH)](98)
3142	3157	3009	3010_{vw}	2997_{vw}	3008, 3008	$\nu_a(CH_3)$(99)
3116	3147	2985	2995_{vw}	2995_{vw}	2984, 2984	R1[$\nu_a(CH_2)$](99)
3072	3093	2945	2958_{vw}	2962_{vw}	2944, 2944	$\nu_a(CH_3)$(99)
3010	3061	2888	2918_{vw}	2891_{vw}	2888, 2888	$\nu_s(CH_3)$(99)
3007	3035	2886	2850_{vw}	2878_{vw}	2885, 2885	R1[$\nu_s(CH_2)$](99)
1801	1947	1764	1687_{vs}	1688_{vw}	1708, 1663	ν(C=O)(77) + R2[ν(C15C24)](5)
1662	1812	1632	1626_{w}	1624_{m}	1631, 1630	R3[ν(CC)(31) + δ_{in}(CH)(9) + δ'_a(5)] + R1[ν(CC)](7) + R2[ν(CC)](8) + $\nu_a(NO_2)$(6)
1645	1766	1615	1624_{w}	1609_{m}	1625, 1615	R4[ν(CC)(45) + δ_a(7) + δ_{in}(CH)(6)] + R1[ν(CC)](6)
1631	1761	1602	1593_{s}	1593_{m}	1602, 1601	R2[ν(CC)(19) + δ_a(5)] + R1[ν(CC)](18) + R4[ν(CC)](14) + R3[ν(CC)](5)
1625	1745	1596	1591_{s}	1591_{m}	1596, 1596	R2[ν(CC)(45) + δ'_a(9) + δ_{in}(CH)(6)] + R3[ν(CC)](5) + R1[δ'_{ring}](5)
1604	1741	1576	1541_{w}	1543_{m}	1575, 1574	$\nu_a(NO_2)$(70)
1577	1686	1550	1539_{w}	1541_{m}	1550, 1550	R3[ν(CC)](25) + R4[ν(CC)(21) + δ_{in}(CH)(9)] + R2[ν(CC)](9)
1544	1653	1518	1523_{s}	1507_{vw}	1519, 1519	R1[$\delta(CH_2)$](91)
1524	1628	1500	1508_{w}	1495_{vw}	1500, 1500	R3[ν(CC)](25) + R4[ν(CC)(11) + δ_{in}(CH)(11)] + R3[δ_a](7)
1505	1608	1481	–		1481, 1481	[δ'_a(56) + δ(22) + ρ(10)](CH_3)
1501	1600	1477	1469_{m}	1468_{vw}	1477, 1477, 1477	δ_s(CH3)(25) + R4[δ_{in}(CH)(26) + ν(CC)(16) + ν(CO)(8)]
1493	1598	1469	1468_{m}	1466_{vw}	1470, 1470	[δ_a(66) + δ'_a(27) + ρ′(6)](CH_3)
1473	1593	1451	1450_{m}	1451_{m}	1458	$\delta_s(CH_3)$(32) + R2[ν(CC)](19) + R1[ν(CO)](6)
1469	1575	1447	1437_{vw}	1449_{m}	1450, 1548, 1545	$\delta_s(CH_3)$(24) + R3[ν(CC)](15) + R4[δ_{in}(CH)(12) + ν(CC)(6)] + R2[ν(CC)](9)
1437	1570	1416	1419_{m}	1406_{m}	1416, 1416	R1[ω(CH_2)(65) + ν(CO)(5)] + R2[δ_{trig}](5)
1412	1545	1392	–	1391_{w}	1391, 1391	R3[ν(CC)(24) + δ_{in}(CH)(9)] + R2[ν(CC)](11) + R4[δ_{in}(CH)(8) + ν(CC)(7)]
1403	1511	1383	1373_{w}	1372_{m}	1437	R2[ν(C15C24)(12) + ν(CC)(14)] + R3[ν(CC)](6) + R1[ν(CO)(6) + ω(CH_2)(6)] + δ(C24HO)(6) + ν(C24O)(5)
1380	1498	1361	1350_{vs}	1350_{vs}	1362, 1361	$\nu_s(NO_2)$(33) + R4[ν(CC)](15) + R3[ν(CC)(10) + ν(CN)(6)] + δ(NO_2)(8)
1377	1475	1358	1348_{vs}	1348_{vs}	1373, 1372	R2[ν(CC)(23) + δ_{in}(C15C24)(6)] + R3[ν(CC)](15) + $\nu_s(NO_2)$(14) + R1[ν(CC)](5)
1365	1427	1346	–	1347_{vs}	1355, 1354, 1346	R4[ν(CC)(31) + δ_{in}(CH)(6)] + R3[ν(CC)(10) + δ_{in}(CH)(7)] + $\nu_s(NO_2)$(10)
1351	1398	1333	1331_{vw}	1331_{vs}	1344	R2[ν(CC)](43) + δ(C24HO)(8) + R1[ν(CC)](8) + R3[ν(CC)](5)
1313	1385	1297	–	–	1316, 1315	R3[ν(CC)](28) + δ(C24HO)(10) + R4[δ_{trig}](8) + ν(CC)(8)] + R2[δ_{trig}(6) + δ_{in}(CH)(5)]
1297	1367	1281	1273_{s}	1271_{m}	1280,1280, 1277, 1273	R4[ν(CO)(33) + δ_{in}(CH)(20) + δ_{trig}(8)] + $\delta_s(CH_3)$(5)
1273	1330	1257	1248_{vs}	1246_{m}	1257, 1256	R3[ν(CC)](24) + R2[ν(CC)(19) + δ_{in}(CH)(5)] + R1[ν(CO)](12) + R4[δ_{in}(CH)(6) + δ_{trig})(4)]
1250	1325	1235	1246_{vs}	1227_{vw}	1235, 1235	R4[ν(CC)(32) + δ_{in}(CH)(10) + ν(CO)(5)] + R3[δ_{in}(CH)(17) + ν(CC)(8)]
1220	1310	1206	1205_{w}	1196_{w}	1204,1204	R4[δ_{in}(CH)](31) + R1[γ(CH_2)(19) + ν(CO)(5)] + ρ(CH_3)(11)
1217	1299	1203	1203_{w}	1194_{w}	1202,1202	R1[γ(CH_2)](65) + ρ(CH_3)(13) + R4[δ_{in}(CH)](9)
1206	1282	1192	–	1192_{w}	1193,1193	ρ(CH_3)(36) + R2[δ_{in}(CH)](17) + R4[δ_{in}(CH)](8) + R1[γ(CH_2)](7)
1195	1274	1183	1171_{vw}	1173_{vw}	1183, 1183	R2[δ_{in}(CH)(19) + ν(CC)(7)] + R3[δ_{in}(CH)(14) + ν(CC)(7)] + ρ(CH_3)(13) + R4[δ_{in}(CH)](9)
1192	1267	1179	1169_{vw}	1171_{vw}	981, 943	δ(C24HO)(20) + R2[δ_{trig}(11) + ν(C15C24)(7)] + ν(C24O)(14) + R3[δ_{trig}](10) + R4[δ_{in}(CH)](6)
1171	1258	1159	1149_{m}	1148_{w}	1159, 1159	ρ′(CH_3)(94)
1150	1245	1139	1147_{m}	1142_{w}	1155, 1153	R1[ρ(CH_2)(23) + ν(CO)(6)] + R3[δ_{trig}](9) + ν(C24O)(8) + ν(C25O)(7) + δ(C24HO)(5)
1145	1234	1134	1126_{m}	–	1148, 1148	R1[ρ(CH_2)](54) + ν(C24O)(7)
1129	1202	1118	1124_{m}	1115_{w}	1124, 1123	ν(C24O)(13) + R4[ν(CC)(11) + δ_{in}(CH)(11) + δ_{trig})(5)] + R2[δ_{trig}](8) + R1[ν(CO)](7) + R3[δ_{in}(CH)](6)
1102	1178	1092	1080_{vw}	1088_{vw}	1092, 1092	R4[ν(CC)(30) + δ_{in}(CH)(8)] + ν(C25O)(13) + R1[ν(CO)](10)
1078	1164	1068	1065w	1067_{w}	1069, 1069	ν(C25O)(27) + R1[ν(CO)](23) + R3[δ_{in}(CH)(5) + ν(CN)(5)]
1058	1130	1049	1043_{s}	1040_{w}	1055, 1054	R1[ν(CO)](37) + R2[ν(CC)](10) + R3[ν(CN)(7) + δ_{in}(CH)(7)] + R1[δ_{ring}](6) + ν(C24O)(6)
1011	1116	1004	999_{w}	1001_{vw}	1008, 1008	ν(C25O)(16) + R1[ν(CO)](13) + R3[δ_{trig}](12) + R1[ν(CO)](8) + R2[δ'_a](7) + R4[δ_{trig})](6)
981	1095	974	–	980_{vw}	975, 975	R4[oop(CH)(84) + puck(6)]
960	1082	953	945_{w}	947_{vw}	956, 956	R1[ν(CO)(51) + δ'_{ring}(6)] + R3[ν(CN)](6) + R2[δ'_a](5)
949	1060	943	943_{w}	945_{vw}	943, 943	R3[oop(CH)(74) + puck(8)]
945	1029	939	941_{w}	928_{vw}	939, 939	R1[ν(CO)](36) + R3[ν(CN)(6) + oop(CH)(6) + δ'_a(5)]
902	1011	896	901_{w}	897_{vw}	901, 901	R2[oop(CH)](82) + τ_a(6) + puck(6)]
887	984	881	879_{vw}	–	883, 883	R4[δ_{trig}(20) + oop(CH)(13) + δ'_a(5)] + R3[ν(CC)(12) + δ_{in}(CH)(8) + δ_{trig}(5) + δ(NO_2)(8)
885	955	880	877_{vw}	872_{vw}	880, 880	R4[oop(CH)(73) + oop(C20O)(5) + τ_a(5)]
853	917	849	841_{w}	845_{vw}	856, 854	R1[ν(CO)](16) + R3[δ_a](11) + δ(NO_2)(9) + R2[ν(CC)(8) + ν(C15C24)(6)] + R4[δ_a)](5)
830	899	826	813_{w}	830_{vw}	827, 827	δ(NO_2)(21) + R4[δ_{trig}(13) + δ'_a(8) + ν(CO)(5)] + R3[δ_a(5) + δ_{in}(CH)(5)] + R2[δ_a](6)
803	890	800	812_{w}	812_{vw}	800,800	R4[puck(33) + oop(CH)(29) + oop(C20O)(12)] + R3[puck](11) + R2[τ'_a](6)
800	885	796	789_{w}	797_{vw}	800, 800	ω(C=O)(40) + R2[oop(C15C24)(17) + δ_{in}(C15C24)(6)]
778	875	775	777_{vw}	778_{w}	782, 778	ω(NO_2)(24) + R3[oop(CN)](17) + R2[τ'_a](5)
775	835	772	766_{w}	770_{w}	775, 775	R1[δ_{ring}](18) + R2[oop(C15C24)](9) + R3[oop(CN)](6) + ω(NO_2)(6) + R2[δ_{trig}](6) + ω(C=O)(5)
753	828	750	754_{m}	756_{vw}	756,754	R1[δ'_{ring}](25) + R1[δ_{ring}](18) + R4[puck(6) + oop(CH)(5)] + R3[puck](6)
752	819	749	752_{m}	745_{vw}	749, 749	R3[puck](27) + R4[puck(21) + oop(CH)(17)] + R2[puck](5)
731	805	729	729_{vw}	727_{vw}	731, 729	R3[puck(12) + oop(CN)(12) + δ_a(8) + δ_{in}(CH)(5)] + R2[puck](10) + R2[τ'_a](6)
712	782	710	714_{vw}	726_{vw}	712, 711	R2[puck(51) + oop(C15C24)(8)] + ω(NO_2)(5)
703	767	701	700_{m}	702_{vw}	706, 705	R2[puck(12) + τ'_a(9) + δ_{in}(C15C24)(5)] + R3[δ_a(6) + puck(5)] + R1[δ'_{ring}](7)
682	747	680	675_{w}	683_{w}	688, 680	R2[τ'_a(27) + τ'_a(5)] + R3[oop(CN)(9) + puck(6)] + τ(C9C10)(9) + R1[τ](6)
656	713	654	–	648_{vw}	678, 678	δ(C=O)(32) + R4[δ_a)](16) + R3[δ_{trig}](6) + δ(C24HO)(5)

(*continued on next page*)

Table 4 (*continued*)

Unscaled DFT	Scaled		Experimental		Dimer	PED[a] (%)
	HF	DFT	IR	Raman	Scaled DFT	
645	708	644	631_{vw}	633_{vw}	640, 640	R4[oop(C20O)(21) + (τ_a + τ'_a)(12)] + τ(C11C13)(15) + R3[puck](13) + R2[oop(C15C24)(7) + puck(7) + τ_a(6)]
618	664	617	621_{w}	619_{vw}	622, 621	R4[δ_a)](18) + R2[δ_a(16) + oop(C15C24)(5)] + τ(C24O)(12) + δ(C=O)(11)
611	657	610	707_{vw}	600_{vw}	981, 936	τ(C24O)(14) + R3[oop(CN)](12) + δ(C20C25O)(9) + R4[δ_{in}(C20O)](8) + R2[τ'_a(7) + oop(C15C24)(6)]
597	637	596	594_{w}	589_{vw}	605, 604	τ(C24O)(15) + R3[δ'_a + δ_a](15) + R4[δ'_a(8) + δ_a)(8) + δ_{in}(C20O)(5)] + δ(C20C25O)(9)
564	613	563	561_{vw}	552_{vw}	571, 567	R4[τ'_a(17) + puck(15) + R3[puck](13) + ρ(NO_2)(6) + ρ(C=O)(5) + R2[τ_a](5)
542	586	542	530_{w}	–	557, 556	R2[τ'_a(13) + τ_a(13) + puck(9)] + R3[oop(CN)](8) + τ(C24O)(7) + R4[τ_a](5) + ρ(NO_2)(5)
518	560	518	–	521_{vw}	523, 519	R4[δ'_a)(14) + τ'_a(10) + puck(5)] + R3[oop(CN)](11) + τ(C9C10)(8) + R2[τ'_a(8) + τ_a(6)]
511	557	511	507_{w}	504_{vw}	517, 517	R2[τ_a(29) + τ'_a(6) + oop(C15C24)(9)] + τ(C12C16)(9) + R4[τ_a](9) + oop(C20O)(7)]
492	528	492	486_{vw}	492_{vw}	496	R3[oop(CN)(11) + δ_a(7)] + R2[τ'_a](11) + R4[δ_a(7) + δ'_a(6) + δ_{in}(C20O)(5)]
423	459	423	420_{vw}	430_{vw}	448, 433	ρ(C=O)(18) + R2[δ'_a(12) + puck(7) + τ_a(6) + ν(CC)(5)] + R1[ν(CO)](5)
395	433	396	–	402_{vw}	401, 398	ρ(NO_2)(14) + R2[τ_a(11) + τ_a(10)] + ρ(C=O)(5) + R4[τ'_a + τ_a](8)
365	391	366	–	–	385, 367	R2[δ_a(21) + δ'_a(19) + ν(C15C24)(5)] + R3[δ_a](15)
345	376	346	–	344_{vw}	354, 351	τ(C12C16)(13) + R3[δ'_a + δ_a](13) + τ(C9C10)(9) + R2[τ_a](5)
336	366	337	–	–	348, 339	τ(C12C16)(20) + R2[oop(C15C24)(10) + τ_a(5)] + R3[ν(CN)](8) + τ(C9C10)(7) + R1[τ](7)
318	341	319	–	–	326, 322, 314	δ(C20C25O)(27) + τ(C12C16)(7) + R3[δ'_a](7) + τ(C9C10)(5)
305	334	306	–	307_{vw}	307	R2[τ_a](12) + τ(C11C13)(10) + R3[oop(CN)(10) + puck(9)] + R4[τ_a](9) + R2[τ'_a](8) + R1[τ'](5)
297	325	298	–	288_{vw}	302, 300	R3[oop(CN)](21) + τ(C25O)(11) + R4[oop(CH)(9) + τ_a(8)] + R2[τ'_a + τ_a(9) + oop(C15C24)(6)]
275	296	276	–	286_{vw}	289, 288	R3[δ'_a](17) + ρ(C=O)(7) + τ(C11C13)(5) + R2[τ'_a + τ_a](7)
255	282	256	–	–	256, 256	τ(C25O)(54) + R4[τ'_a](14) + R3[oop(CN)](5)
240	258	241	–	243_{vw}	244, 242	R4[δ_{in}(C20O)](17) + R3[δ_{in}(CN)(12) + δ_{trig}(6) + oop(CN)(5)] + τ(C12C16)(7) + δ(C20C25O)(6) + R2[ν(CC)](5)
200	219	201	–	199_{vw}	206, 201	τ(C12C16)(19) + R2[τ'_a(10) + oop(C15C24)(5)] + R1[τ](10) + τ(C11C13)(10) + R4[τ_a](6) + τ(CN)(6) + R3[δ_{in}(CN)](5)
195	215	196	–	–	198, 196	R4[τ_a(18) + τ'_a(15)] + R2[δ_{in}(C15C24)(8) + oop(C15C24)(7) + puck(5)] + τ(C25O)(8) + τ(C12C16)(7)
188	207	189	–	–	190, 189	R4[τ'_a + τ_a](23) + R2[δ_{in}(C15C24)](13) + R1[τ](6) + τ(C12C16)(5) + R3[oop(CN)](5)
181	196	182	–	–	189,187	τ(C11C13)(15) + τ(C12C16)(10) + R2[τ'_a(9) + oop(C15C24)(8) + δ_{in}(C15C24)(7)] + τ(C20O)(5)
137	154	137	–	151_{vw}	156, 143, 140, 137	R1[τ'](25) + R1[τ](17) + R3[δ_{in}(CN)](9) + R4[δ_{in}(C20O)](6) + R2[oop(C15C24)](5)
129	145	130	–	130_{m}	128, 121	R1[τ' + τ(67)] + R2[oop(C15C24)](5)
107	122	108	–	–	108, 107	R2[τ'_a(20) + δ_{in}(C15C24)(7)] + τ(C12C16)(11) + τ(C20O)(11) + τ(CN)(11) + τ(C25O)(5)
105	114	105	–	–	103, 101, 96	τ(C20O)(18) + τ(CN)(15) + R2[τ'_a](10) + τ(C12C16)(8) + τ(C25O)(7) + τ(C15C24)(6) + τ(C11C13)(5)
90	99	90	–	85_{s}	86,85	R1[τ) + τ'](56) + τ(CN)(9) + τ(C20O)(8 + R2[oop(C15C24)(6) + τ'_a(6)]
82	89	83	–	83_{s}	82, 78	τ(C20O)(16) + R2[τ'_a(14) + R2[oop(C15C24)](5) + τ(CN)(12) + R1[τ' + τ](21) + R3[oop(CN)](7)
71	79	72	–	–	53, 52	τ(C15C24)(52) + τ(CN)(19) + τ(C20O)(5)
42	46	42	–	41_{m}	44, 43	R2[τ'_a + τ_a](38) + τ(C9C10)(18) + τ(C11C13)(12) + R4[τ'_a](6) + R3[puck](6)
35	40	36	–	–	34, 24, 16, 9, 6	τ(C15C24)(24) + R2[τ'_a(24) + τ_a(13)] + τ(C9C10)(11) + τ(CN)(8) + τ(C11C13)(7)

Proposed assignments and potential energy distribution (PED) for vibrational normal modes Types of vibration: ν, stretching; δ, deformation (bending), scissoring; oop, out-of-plane bending; ω, wagging; γ, twisting; ρ, rocking; τ, torsion; w, weak; vw, very weak; m, medium; s, strong; vs very strong.

[a] Potential energy distribution (contribution ⩾5).

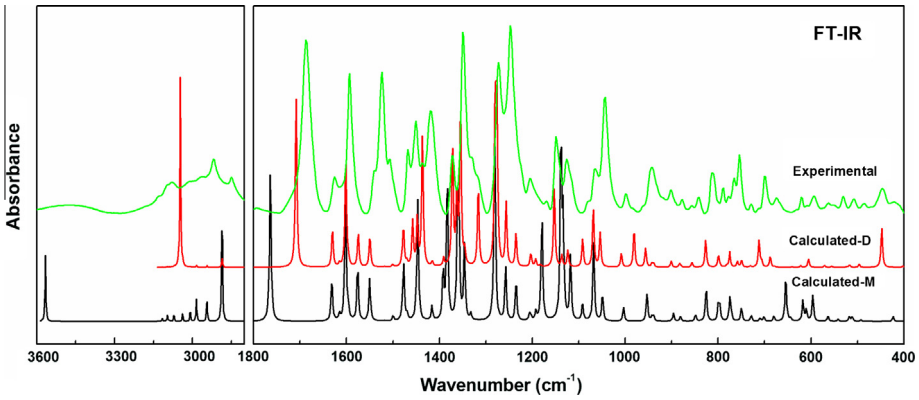

Fig. 5. Observed and calculated (scaled) IR absorption spectra of AA I in the region; 3600–2800 cm^{-1} and 1800–400 cm^{-1}.

puckering modes are calculated at 710/701 cm^{-1}. These modes are observed at 714/700 cm^{-1} in the IR spectrum and at 726/702 cm^{-1} in the Raman spectrum, respectively.

Ring R3 vibrations

The six membered ring R3 has a CH and one NO_2 moiety. The C—H stretching vibration is calculated at 3097 cm^{-1} and observed at 3095 cm^{-1} in the IR spectrum and at 3098 cm^{-1} in the Raman spectrum. The out-of-plane deformations are calculated at 492 and 298 cm^{-1}, which is observed in the bands at 486 cm^{-1} in the IR and at 492 and 288 cm^{-1} in the Raman spectrum, respectively. The in-plane deformation and torsion of C—N are obtained below 500 cm^{-1} with low contributions.

Ring R4 vibrations

Ring R4 is also a benzene ring with three CH moieties and an O—CH_3 (methoxy) group, connected with it. Three C—H stretching modes are calculated at 3116, 3072 and 3038 cm^{-1} associated with

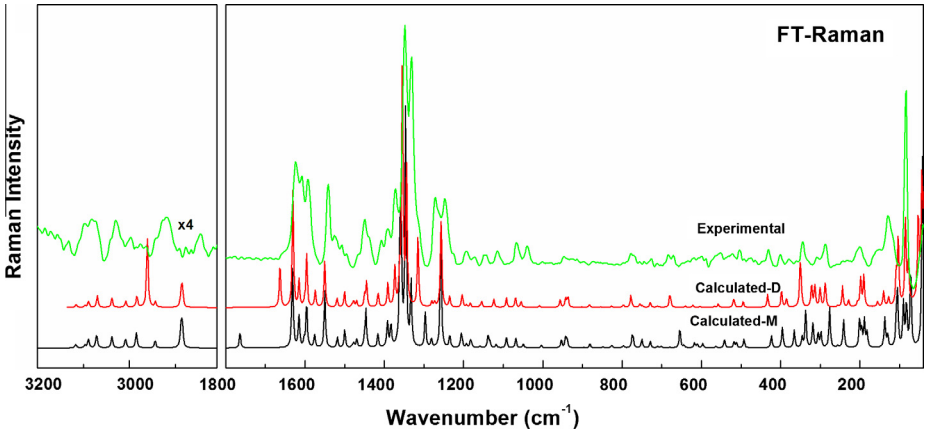

Fig. 6. Observed and calculated (scaled) Raman intensity spectra of AA I in the region; 3700–2800 cm^{-1} and 1800–50 cm^{-1}.

this ring. These pure modes have good agreement with the observed frequencies. The CH in-plane deformations are calculated at 1477 and 1206 cm^{-1}, which matches well with 1469 and 1205 cm^{-1} in the IR spectrum and at 1468 and 1196 cm^{-1} in the Raman spectrum. The CH out-of-plane deformations are calculated at 974, 880, and 644 cm^{-1}.

The C—O stretching is calculated at 1281 cm^{-1}, corresponding to the observed strong band at 1273 cm^{-1} in the IR spectrum and at the medium intensity band at 1271 cm^{-1} in the Raman spectrum. The out-of-plane deformation is calculated at 644 cm^{-1} and is observed at 631 cm^{-1} in the IR spectrum and at 633 cm^{-1} in the Raman spectrum.

The trigonal deformation, puckering, asymmetric torsion and asymmetric deformations of the ring were calculated at 881, 800, 563 and 518 cm^{-1}, respectively.

Conclusion

The equilibrium geometries and harmonic vibrational wavenumbers of all the 102 normal modes of the AA I molecule were determined and analyzed both at DFT (B3LYP) and HF levels of theory employing the 6-311G(d,p) basis set. These vibrational assignments along with the electronic transitions are important to understand the molecular structure and biological activity of the title molecule. The Raman and IR spectra have been recorded, and compared with the calculated one on the basis of the PED analysis. Both the observed and calculated wavenumbers have been found in good agreements. The agreement in OH stretching is better in dimer than in the monomer. The frequency difference in monomer is 439 cm^{-1} which reduces to ≈81 cm^{-1} in the dimer due to the formation of intermolecular H-bonding O—H···O═C. On moving from monomer to dimer, the bond lengths O—H and C═O increase by 0.03186 and 0.02125 Å, respectively. But the bond length C24—O decreases by 0.03747 Å in dimer than in monomer. These structural changes support that the dimer is more stable structural form indeed. Information about the size, shape, charge density distribution and structure–activity relationship of the AA I molecule has been obtained by mapping electron density isosurface with ESP and MESP. The UV spectrum was measured in ethanol solution and compared with theoretical values in the gas phase and in ethanol environment (IEF-PCM model) using TD-DFT//B3LYP/6-31G basis set, shows the charge transfer within the molecule. HOMO–LUMO plot elucidate the involvement of molecule in charge transfer between the donor and acceptor groups. The NBO analysis reveals hyper conjugative interaction, ICT and stabilization of the molecule. Variation of the thermodynamic properties with the temperature is due to increase in molecular vibrational intensities. The MESP surface drawn, molecular orbitals and the electronic transitions identified for UV–vis spectra may lead to the understanding of structure properties and activity of AA I. All the thermodynamic properties increase due to the rise in temperature because of increase in molecular vibrations. The DSC curve observed on heating shows a sharp melting point at 268.99 °C.

Acknowledgements

B.D. Joshi would like to thank the U.G.C., Nepal, for providing partial fellowship. A.S. thanks CSIR, New Delhi, for financial assistance in the form of a Research Associateship (R.A.). V.G. acknowledges the financial support provided by the U.G.C., India under the U.G.C.-Dr. D.S. Kothari Postdoctoral Fellowship.

Appendix A. Supplementary material

Supplementary data associated with this article can be found, in the online version, at http://dx.doi.org/10.1016/j.saa.2013.07.036.

References

[1] G. Krumbiegel, J. Hallensleben, W.H. Mennicke, et al., Xenobiotica 17 (8) (1987) 981–991.
[2] D. Bensky, A. Gamble, T. Kaptchuk, L.L. Bensky, Chinese Herbal Medicine: Materia Medica, revised ed., Eastland Press Washington, USA, 1993. pp. 136.
[3] W. Tang, G. Eisenbrand, Chinese Drugs of Plant Origin-chemistry, Pharmacology and Use in Traditional and Modern Medicine, Springer-Verlag, Berlin, Germany, 1992. pp. 145.
[4] M. Mizuno, T. Oka, H. Yamamoto, M. Iinuma, H. Murata, Chem. Pharm. Bull. 39 (1991) 1310–1311.
[5] S.M. Kupchan, R.W. Doscoth, J. Med. Pharm. Chem. 5 (1962) 657–659.
[6] G.M. Lord, R. Tagore, T. Cook, P. Gower, C.D. Pusey, Lancet 354 (1999) 481–482.
[7] G.M. Lord, T. Cook, V.M. Arlt, H.H. Schneider, G. Williams, C.D. Pusey, Lancet 358 (2001) 1515–1516.
[8] W. Pfau, H.H. Schmeiser, M. Wiessler, Carcinogenesis 11 (1990) 313–319.
[9] S. Attaluri, R.R. Bonala, I.-Y. Yang, M.A. Lukin, Y. Wen, A.P. Grollman, M. Moriya, C.R. Iden, F. Johnson, Nucleic Acids Res. 38 (1) (2010) 339–352.
[10] V.M. Arlt, M. Stiborová, J. Brocke, et al., Carcinogenesis 28 (2007) 2253–2261.
[11] Y.T. Hong, L.S. Fu, L.H. Chung, S.C. Hung, Y.T. Huang, C.S. Chi, Pediatr. Nephrol. 21 (2006) 577–579.
[12] P. Balachandran, F. Wei, R.C. Lin, I.A. Khan, D.S. Pasco, Kidney Int. 67 (2005) 1797–1805.
[13] J.M. Chamers, P.R. Griffiths, Handbook of Vibrational Spectroscopy, John Wiley and Sons, New York, 2002.
[14] R.S. Lebedev, Russ. Phys. J. 45 (2002) 822–830.
[15] I. Kostova, I. Hubert Joe, S. Cinta Pinzaru, J. Optoelectron. Biomed. Mater. 1 (2009) 188–199.
[16] A.P. Ayala, H.W. Siesler, S.M.H.V. Wardell, N. Boechat, V. Dabbene, S.L. Cuffini, J. Mol. Struct. 828 (2007) 201–210.
[17] S. Mishra, D. Chaturvedi, P. Tandon, V.P. Gupta, A.P. Ayala, S.B. Honorato, H.W. Siesler, J. Phys. Chem. A 113 (2009) 273–281.
[18] G. Dinorah, O Lucia, M Vieites, M Boiani, M Gonzalez, E.J. Baran, H. Cerecetto, Spectrochim. Acta A 68 (2007) 341–348.

[19] H.R.H. Ali, H.G.M. Edwards, J. Kendrick, I.J. Scowen, Spectrochim. Acta A 72 (4) (2009) 715–719.
[20] V. Gupta, K.S. Smirnov, D. Bougeard, P. Tandon, J. Chem. Theory Comput. 5 (5) (2009) 1369–1379.
[21] A. Sharma, V. Gupta, R. Mishra, P. Tandon, S. Maeda, Ko-Ki Kunimoto, J. Mol. Struct. 1004 (2011) 237–247.
[22] D. Chaturvedi, V. Gupta, P Tandon, A. Sharma, C. Baraldi, M.C. Gamberini, Spectrochim. Acta A 99 (2012) 150–159.
[23] B.D. Joshi, A. Srivastava, S.B. Honorato, P. Tandon, O.D.L. Pessoa, P.B.A. Fechine, A.P. Ayala, Spectrochim. Acta A 113 (2013) 367–377.
[24] Y. Gong, Y. Lu, Q. Zheng, Acta Crystallogr. E 63 (2007) 04836.
[25] P. Hohenberg, W. Kohn, Phys. Rev. B 136 (1964) 864–871.
[26] M.J. Frisch, G.W. Trucks, H.B. Schlegel. G.E. Scuseria, J.R. Cheeseman, M.A. Robb, G. Scalmani, V. Barone, B. Mennucci, G.A. Petersson, H. Nakatsuji, M. Caricato, X. Li, H.P. Hratchian, A.F. Izmzylov, J. Bloino, G. Zheng, J.L. Sonnenberg, M. Hada, M. Ehara, K. Toyota, R. Fukuda, J. Ishida, M. Hasegawa, T. Nakajima, Y. Honda, O. Kitao, H. Nakai, T. Vreven, J.A. Montgomery Jr., J.E. Peralta, F. Ogliaro, M. Bearpark, J.J. Heyd, E. Brothers, K.N. Kudin, V.N. Staroverov, R. Kobayashi, J. Normand, A. Raghavachari, A. Rendell, J.C. Burant, S.S. Iyengar, J. Tomasi, M. Cossi, N. Rega, J.M. M illan, M. Klene, J.E. Knox, J.B. Cross, V. Bakken, C. Adamo, J. Jaramillo, R. Gomperts, R.E. Stratmann, O. Yazyev, A.J. Austin, R. Cammi, C. Pomelli, J.W. Ochterski, R.L. Martin, K. Morokuma, V.G. Zakrzewski, G.A. Voth, P. Salvador, J.J. Dannerberg, S. Dapprich, A.D. Daniels, J. Farkas, B. Foresman, J.V. Ortiz, J. Cioslowski, D.J. Fox, Gaussian 09, Revision, Gaussian, Inc., Wallingford, CT, 2009.
[27] C.T. Lee, W. Yang, R.G. Parr, Phys. Rev. B 37 (1998) 785–789.
[28] R.G. Parr, W. Yang, Density Functional Theory of Atoms and Molecules, Oxford University Press, New York, 1989.
[29] A.D. Becke, J Chem. Phys. 98 (1993) 5648–5652.
[30] G.A. Petersson, M.A. Allaham, J. Chem. Phys. 94 (1991) 6081–6090.
[31] G.A. Petersson, A. Bennett, T.G. Tensfeldt, M.A. Allaham, W.A. Shirley, J. Mantzaris, J. Chem. Phys. 89 (1988) 2193–2218.
[32] P. Pulay, G. Fogarasi, F. Pang, J.E. Boggs, J. Am. Chem. Soc. 101 (1979) 2550–2560.
[33] G. Fogarasi, X. Zhou, P.W. Taylor, P. Pulay, J. Am. Chem. Soc. 114 (1992) 8191–8202.
[34] J.M.L. Martin, C.V. Alsenoy, GAR2PED, University of Antwerp, 1995.
[35] G.A. Zhurko, D.A. Zhurko, Chemcraft, 2005. <http://www.chemcraftprog.com>.
[36] P. Politzer, D.G. Truhlar, Chemical Applications of Atomic and Molecular Electrostatic Potentials, Plenum, New York, 1981.
[37] S.R. Gadre, P.K. Bhadane, S.S. Pundlik, S.S. Pingale, in: J.S. Murray, K.D. Sen (Eds.), Molecular Electrostatic Potentials Concepts and Applications, 1996, pp. 219–255.
[38] P. Politzer, M.E. Grice, J.S. Murray, J.M. Seminario, Can. J. Chem. 71 (1993) 1123–1127.
[39] C.H. Suresh, P. Alexander, K.P. Vijayalakshmi, P.K. Sajith, S.R. Gadre, Phys. Chem. Chem. Phys. 10 (2008) 6492–6499.
[40] P. Balnarayan, S.R. Gadre, J. Chem. Phys. 119 (2003) 5037–5043.
[41] A. Srivastava, P. Tandon, A.P. Ayala, S. Jain, Vib. Spectrosc. 56 (2011) 82–88.
[42] A. Srivastava, P. Tandon, S. Jain, B.P. Asthana, Spectrochim. Acta A 84 (2011) 144–155.
[43] R.M. Issa, M.K. Awad, F.M. Atlam, Appl. Surf. Sci. 255 (2008) 2433–2441.
[44] E.D. Glendening, A.E. Reed, J.E. Carpenter, F. Weinhold, NBO Version 3.1, TCI, University of Wisconsin, Madison, 1998.
[45] F. Weinhold, C.R. Landis, Valency and Bonding: A Natural Bond Orbital Donor–Acceptor Perspective, Cambridge University Press, New York, 2005.
[46] F. Weinhold, C.R. Landis, Chem. Educ. Res. Pract. 2 (2001) 91–104.
[47] A.E. Reed, L.A. Curtiss, F. Weinhold, Chem. Rev. 88 (1988) 899–926.
[48] B. Yin, G. Wang, S.N. Niya, Y. Huang, J. Mol. Model. 14 (2008) 789–795.
[49] A. Borrego, G. Gonzalez-Doncel, Mater. Sci. Eng., A 245 (1998) 10–18.
[50] J. Vazquez, P. Villares, R. Jimenez-Garay, J. Alloys Compd. 257 (1997) 259–265.
[51] J. Vazquez, C. Wagner, P. Villares, R. Jimenez-Garay, Acta Mater. 44 (1996) 4807–48013.
[52] H. Yoshida, K. Takeda, J. Okamura, A. Ehara, H. Matsurra, J. Phys. Chem. A 106 (2002) 3580–3586.
[53] M.W. Wong, Chem. Phys. Lett. 256 (1996) 391–399.
[54] A.P. Scott, L. Radom, J. Phys. Chem. 100 (1996) 6502–16513.
[55] G.A. Guirgis, P. Klaboe, S. Shen, D.L. Powell, A. Gruodis, V. Aleksa, C.J. Nielsen, J. Tao, C. Zheng, J.R. Durig, J. Raman. Spectrosc. 34 (2003) 322–336.
[56] P.L. Polavarapu, J. Phys. Chem. 94 (1990) 8106–8112.
[57] M. Rumi, G. Zerbi, J. Mol. Struct. 509 (1999) 11–28.
[58] G.M. Anderson, P.A. Kollman, L.N. Domelsmith, K.N. Houk, J. Am. Chem. Soc. 101 (1979) 2344–2352.
[59] M. Tommasini, C. Castiglioni, M. Del Zoppo, G. Zerbi, J. Mol. Struct. 480 (1999) 179–188.
[60] N. Sundaraganesan, C. Meganathan, H. Saleem, B. Dominic Joshua, Spectrochim. Acta A 68 (2007) 619–625.
[61] Y. Hung, D.F.R. Gilson, I.S. Butler, J. Chem. Phys. 97 (1993) 1998.
[62] K. Bahgat, A.G. Ragheb, Cent. Eur. J. Chem. 5 (2007) 201–220.
[63] N.B. Colthup, I.H. Daily, S.E. Wiberley, Introduction to Infrared and Raman Spectroscopy, Academic Press, New York, 1990.
[64] C.N. Banwell, E.M. McCash, Fundamentals of Molecular Spectroscopy, fourth ed., McGraw-Hill International (UK) Limited, 1994.
[65] S.N. Terekhov, V.S. Chirvonyi, P.Y. Turpin, J. Appl. Spectrosc. 67 (5) (2006) 796–805.
[66] J.P. Abraham, D. Sajan, I. Hubert Joe, V.S. Jayakumar, Spectrochim. Acta, Part A: Mol. Biomol. Spectrosc. 71 (2008) 355–367.
[67] M.C. Ruiz Delgado, V. Hernández, J. Casado, J.T. López Navarrete, J.-M. Raimundo, P. Blanchard, J. Roncali, J. Mol. Struct. 651 (2003) 151–158.
[68] D. Sajan, J. Binoy, B. Pradeep, K. Venkata Krishna, V.B. Kartha, I. Hubert Joe, V.S. Jaykumar, Spectrochim. Acta A 60 (2004) 173–180.
[69] K. Furic, V. Muhacek, M. Bonifacic, I. Stefanic, J. Mol. Struct. 267 (1992) 39–44.
[70] V.K. Rastogi, M.A. Palafox, R.P. Tanwar, L. Mittal, Spectrochim. Acta A 58 (9) (2002) 1987–2004.
[71] M. Silverstein, G.C. Basseler, C. Morill, Spectrometric Identification of Organic Compounds, Wiley, New York, 1981.